

Interaction Between Mineral Phases in a Hematite Iron Ore and Fluxing Materials During Sintering



HUIBIN LI, DAVID J. PINSON, PAUL ZULLI, LIMING LU,
RAYMOND J. LONGBOTTOM, SHENG J. CHEW, BRIAN J. MONAGHAN,
and GUANGQING ZHANG

The interaction between mineral phases in two commercial iron ores and flux materials (CaO, MgO, SiO₂, and Al₂O₃) was studied under 0.5 kPa O₂ partial pressure while heating to different temperatures. CaO was the most effective flux for liquid phase generation during sintering. For a hematite ore with few gangue components (Ore A), the formation of an initial liquid phase commenced at ~1275 °C, with the liquid volume increasing dramatically as temperature increased to 1300 °C. For a goethite containing hematite ore (Ore B), the formation of an initial liquid phase through interaction between goethite and CaO was observed when heating to 1225 °C, with the majority of goethite transformed to liquid at 1250 °C. The porous morphology of sintered goethite and finely distributed quartz results in a high reactivity with CaO. The initial liquid phase penetrated into the pores within the hematite matrix, promoting assimilation and by 1300 °C, all hematite in Ore B was dissolved. The hematite/martite phase in Ore B was much easier to assimilate than that in Ore A due to the presence of goethite. MgO diffused into hematite ore grains by solid-state diffusion and formed a solid solution (Fe, Mg)O•Fe₂O₃ without the formation of a liquid phase. The reaction layer formed by MgO diffusion was limited to approx. 60 μm at 1300 °C. The porous morphology in goethite facilitated MgO diffusion. However, the cavities and cracks caused by goethite dehydration significantly restricted solid phase diffusion of Mg²⁺. There was no observed interaction between Al₂O₃ and SiO₂ with Ores A and B when heated to 1300 °C.

<https://doi.org/10.1007/s11663-020-02010-8>

© The Minerals, Metals & Materials Society and ASM International 2020

I. INTRODUCTION

IRON ore sintering has developed to enable the incorporation of a wide variety of iron ores, *i.e.*, outside traditional hard hematite ores. These ores have mineralogies that may be relatively simple, but the textures are often complex and can negatively influence the performance of ironmaking processes.^[1–3] Hematite ores may be classified into two main types: microplaty hematite and hematite-goethite.^[4] In this investigation, two different hematite ores, Ore A and Ore B, were studied. Ore A is martite-microplaty hematite, while Ore B consists

of a stratiform distribution of martite and goethite.^[4,5] While the characteristics of these hematite ores have been previously described,^[4] no information on the evolution of new mineral phases from the interaction between the mineral phases of iron ores and fluxing materials such as CaO under sintering conditions has been reported in the literature.

Normally, prior to a new blend being used in the sinter plant, bench- or pilot-scale sintering tests are undertaken.^[6–8] For bench-scale experiments, one technique involves ores and fluxes ground into powder, mixed together according to an industrial recipe and pressed into tablets. These tablets are then placed into a furnace at fixed temperature and atmosphere.^[9–14] While accurate control of temperature and atmosphere is achieved in these experiments, a disadvantage is that the effects of particle size and heterogeneity of the blend are neglected. For pilot-scale experiments, the industrial sintering process can be simulated reasonably well. However, both bench- and pilot-scale techniques focus on the properties of the final sinter product, and the interaction of ore mineral phases with fluxing materials is not directly considered.

HUIBIN LI, PAUL ZULLI, RAYMOND J. LONGBOTTOM, BRIAN J. MONAGHAN, and GUANGQING ZHANG are with the ARC Research Hub for Australian Steel Manufacturing, School of Mechanical, Materials Mechatronics and Biomedical Engineering, University of Wollongong, Wollongong, NSW 2500, Australia. Contact e-mail: HL762@uowmail.edu.au DAVID J. PINSON and SHENG J. CHEW are with BlueScope Steel, Port Kembla, NSW 2505, Australia. LIMING LU is with the CSIRO Queensland Center for Advanced Technologies, Brisbane, QLD 4069, Australia.

Manuscript submitted April 3, 2020; accepted October 14, 2020.

Article published online November 4, 2020.

In this study, a novel experimental design was used wherein cubes of iron ore were surrounded by a fluxing material and pressed into tablets. These were sintered and the reaction interfaces examined in detail. The experiments using ore-flux couples allow better understanding of the interaction between individual mineral phases and fluxes under controlled conditions. This investigation fills a knowledge gap concerning the interaction between the mineral phases of representative hematite ores and flux materials (CaO, MgO, Al₂O₃, and SiO₂). A better understanding of the behavior of ore mineral phases is developed, which is helpful for the overall improvement of blending and sinter plant operations in general.

II. EXPERIMENTAL

A. Materials

Table I shows the chemical compositions of the two ores, Ore A and Ore B. The fluxes used, CaO, MgO, SiO₂, and Al₂O₃, were sourced from Sigma-Aldrich Australia with impurity content lower than 0.01 pct. The fluxing materials were generally nano-sized powders. CaO was the coarsest of all the fluxes (particle diameter 98 pct < 160 nm). CaO was calcined at 1000 °C for 12 hours before use.

B. Sample Preparation

Cube-shaped samples of iron ore surrounded by flux material were sintered and used to investigate the interactions of individual mineral phases with fluxes at the interface (Figure 1). To prepare each tablet, a lump of iron ore was cut and polished to form a cube (~ 8 mm sides). The specific cube contains the target mineral phases and reduces the effect of unrelated mineral phases on the interaction during sintering. The cube was centrally placed at the bottom of a die of 16 mm diameter, which was filled with flux powder. A pressure of 25 MPa was applied to form a tablet of 16 mm diameter and ~ 16 mm high (Figure 1(a)). The pressure used aims to ensure intimate contact between the iron ore cube and flux, forming a high-quality tablet without obvious damage to the shape of iron ore lumps.

C. Sintering Procedure

Sintering was carried out in a vertical electric heating tube furnace—the setup is schematically presented in Figure 1(b). The experiments were carried out at atmospheric pressure. A tablet was loaded into a steel wire

basket and located in the furnace hot zone (“sintering zone” in Figure 1(b)). After the set sintering time was reached, the sample was taken out of the furnace and cooled in air.

The overall oxygen partial pressure in the exhaust gas of a sinter strand is high. However, due to the non-uniform gas flow, and the progression of the flame front, the oxygen partial pressure in a sinter bed is dynamic and non-uniform over a large range (0 to 21 pct). In a local area where the gas flow is weak and oxygen is consumed by the combustion of coke, the oxygen partial pressure can be very low. In previous investigations it was shown that 0.5 pct O₂ partial pressure was a representative value for the formation of mineral phases during high temperature sintering, and was determined for tablet sintering conditions to produce similar overall microstructures.^[15–17] The O₂ partial pressure value 0.5 pct was therefore used in this investigation in assessing mineral composition effect in tablet sintering. A sintering atmosphere of 0.5 kPa O₂ partial pressure was maintained by mixing air and nitrogen, with a total gas flow rate of 1 L/min, controlled *via* mass flow controllers.

The sintering time required to heat each sample to the required temperature was determined according to the temperature profile curves of instrumented tablets (Figure 2). These temperature profiles were obtained by pressing the tip of a thermocouple (type R) into the center of an alumina tablet (without an iron ore cube). The tablet was placed in the hot zone at 1300 °C, calibrated in advance using a type R thermocouple, with the tablet temperature recorded using a computer with LabVIEW software. Figure 2 also demonstrates the repeatability of this method for temperature measurement of two tablets. The curves #1 and #2 show the different tablets’ temperature changes during heating, holding, and cooling, in which the holding time was different, while the heating and cooling curves kept same trend exactly. The heating time required for tablets to reach the set temperature was determined from the temperature profile. The times (in seconds) needed to

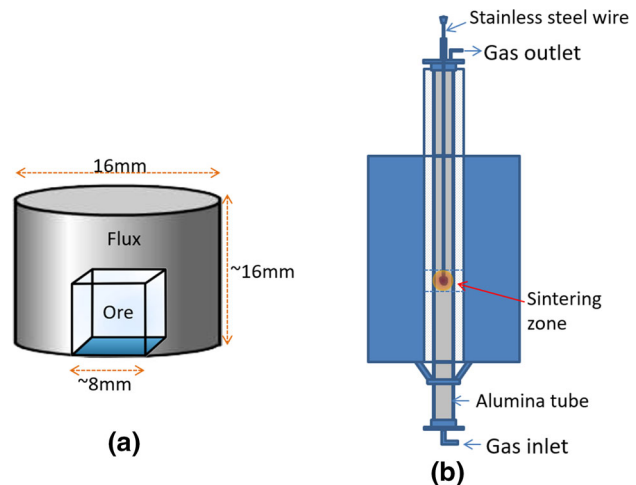


Fig. 1—Schematics of (a) a tablet, and (b) a vertical electrical furnace setup used for interaction experiments.

Table I. Chemical Composition of the Hematite Ores, Weight Pct

Ore	Fe	Al ₂ O ₃	SiO ₂	P	S	LOI
A	65.52	0.98	1.43	0.04	0.006	1.92
B	63.15	1.41	3.44	0.082	0.018	4.42

heat a sample to 1200, 1225, 1250, 1275, and 1300 °C were 122, 134, 156, 194, and 300, respectively. A temperature profile of a sample heated to 1250 °C followed by cooling by withdrawing the tablet from the furnace is shown in Figure 2.

It is worth noting that the tablet experiments were not conducted at all the temperatures noted above, since some of the flux materials had not interacted with ore particles by 1300 °C. For CaO, the full range was used (*i.e.*, 1200 °C to 1300 °C), while for MgO the minimum temperature was 1250 °C (through to 1300 °C). For Al₂O₃ and SiO₂, only 1300 °C was used.

D. Characterization Methods

The sintered tablets were mounted in epoxy resin in preparation for optical and SEM-EDS analysis. After curing, the surface was ground and washed with anhydrous ethanol, then polished to a 1 μm finish for optical microscopic observation (Leica DM6000 Optical Microscope). The polished samples were platinum coated and analyzed by scanning electron microscopy (JEOL JSM-6490LV) operated at 20 kV.

It was challenging to identify the presenting state of some minerals and the interaction process at high sintering temperatures because the observed samples were cooled after reaction, during which solidification of melt phase and segregation of the components by forming new phases may have taken place. However, the indirect information obtained was used for deriving the mineral status at high temperatures. Information on the morphology, homogeneity of the chemical composition, whether the chemical composition matches a compound, and the melting behavior of possible phases according to relevant phase diagrams, was all comprehensively considered.

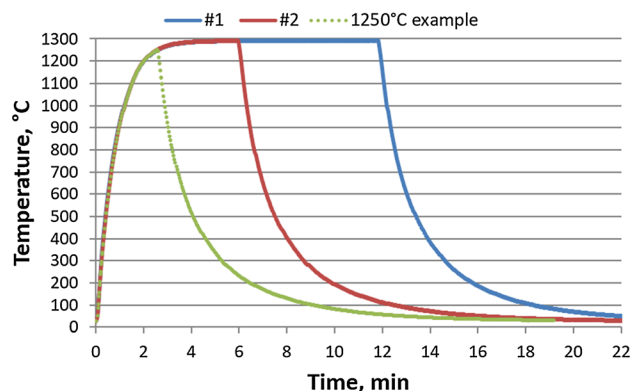


Fig. 2—Temperature profiles of tablets loaded into the furnace set to a final temperature of 1300 °C.

III. RESULTS AND DISCUSSION

A. Interaction Between Hematite Phase in Ore A and Fluxing Materials

1. Hematite and CaO

Figure 3 shows the optical microscopic (OM) images of representative Ore A-CaO tablets after sintering to different temperatures. This figure shows that at higher temperatures (*e.g.*, 1250 °C), gaps were observed between the ore and CaO on some sides. This may be because the CaO and ore body shrank to different extents. However, contact between ore and CaO was maintained on at least two interfaces of the cubes (Figure 3). Similar shrinkage behavior was observed using the other fluxes.

In Figure 3, no changes on contact interfaces were observed for the sample heated to 1250 °C, while a reacted layer was observed between the ore and CaO for the sample heated to 1275 °C (Figure 3, area (b)). When heated to 1300 °C, the majority of the ore was melted, with only a small mass of unreacted ore remaining—survival of this remnant is likely due to the separation between ore and CaO. The evolution of mineral phases during the interaction was further investigated by SEM analysis for areas (a)-(d) in Figure 3.

Figure 4 shows the back-scattered electron (BSE) image and energy-dispersive spectroscopic (EDS) mapping of area (a) marked in Figure 3. The BSE image shows that fine ore particles were retained on the cube edge. These particles were the most reactive during interaction. Their presence in the sintered sample indicates that melting of the ore did not take place. Limited solid-state diffusion of CaO *via* Ca²⁺ and O²⁻ at 1250 °C was confirmed by the chemical composition (Table II) of the sites marked in Figure 4. For example, Site 4, which is close to the edge of the ore particle, had a similar composition to those within the ore particle (Sites 1 to 3). In Table II (and latter tables), the contents of some elements such as Al, Si, and Ca were low and the data are indicative only.

At 1275 °C, a small amount of liquid phase was generated at the interface between ore and CaO. Figure 5 shows the photomicrograph, BSE and EDS mapping of area (b) shown in Figure 3. Although anhydrous ethanol was used in the preparation of the samples, some of the CaO powder were removed from the CaO zone. As a result, the CaO in the sintered sample overlaps with carbon from the mounting resin (Figure 5), giving the appearance that Ca in pure CaO was less than that in C₂F (2CaO·Fe₂O₃). Two layers of reaction products can be observed between the ore and unreacted CaO, with thicknesses of ~ 250 and 20 μm, respectively. The thin layer of reaction product, marked as “initial liquid phase” in Figure 5, was easier to observe in the optical image and the mapping of Ca distribution. The thick layer, marked as “C₂F” in Figure 5, is considered to be a reaction product of penetration of initial liquid phase into the original CaO layer.

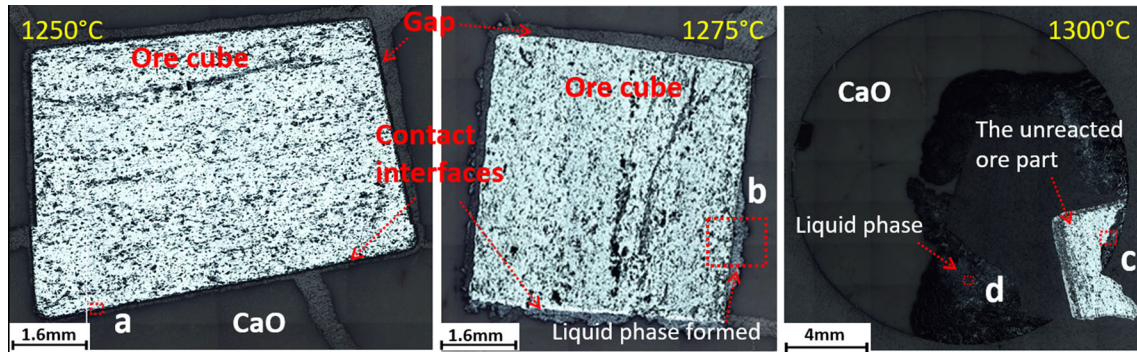


Fig. 3—Photomicrographs of Ore A-CaO tablet heated to 1250, 1275, and 1300 °C.

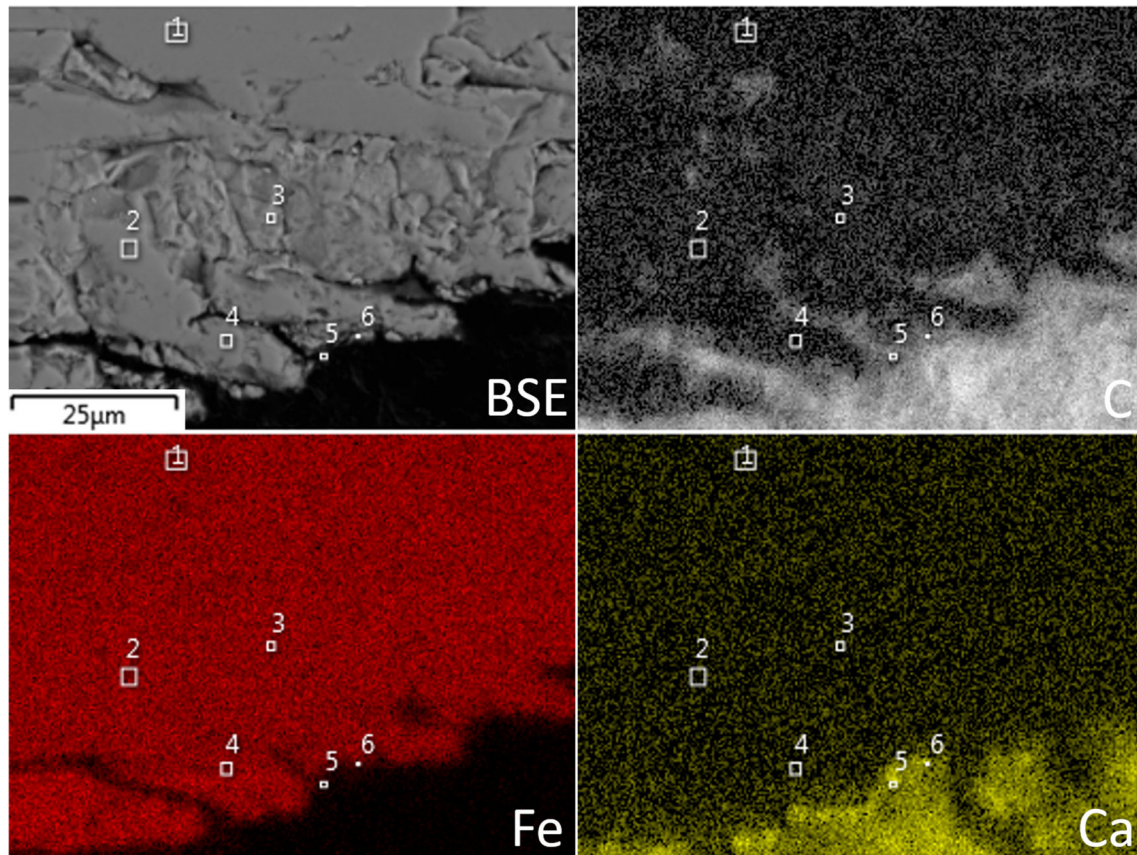


Fig. 4—BSE image and EDS mapping of area (a) in Figure 3.

Table II. Elemental Composition (At. Pct) at the Sites Marked in Figure 4

Site	1	2	3	4
O	64.8	65.3	61.4	64.7
Al	0.07	0.10	0.19	0.10
Si	0.05	0.03	0.03	0.04
Ca	0.05	0.13	0.15	0.30
Fe	35.0	34.5	38.2	34.8
Total	100	100	100	100

To better understand the interaction between the ore and CaO, the area marked as b' in Figure 5 was examined under higher magnification. The corresponding BSE image and Ca and Fe distributions by EDS mapping are presented in Figure 6(a). Three regions may be distinguished in area b', as evidenced, for example, in the Ca distribution map. Some pores are also observed in the right-hand side, in which two phases with slightly different brightness were observed. The compositions of the three regions were identified by the EDS analysis of the sites marked in Figure 6(a), and the results are presented in Table III. The distributions

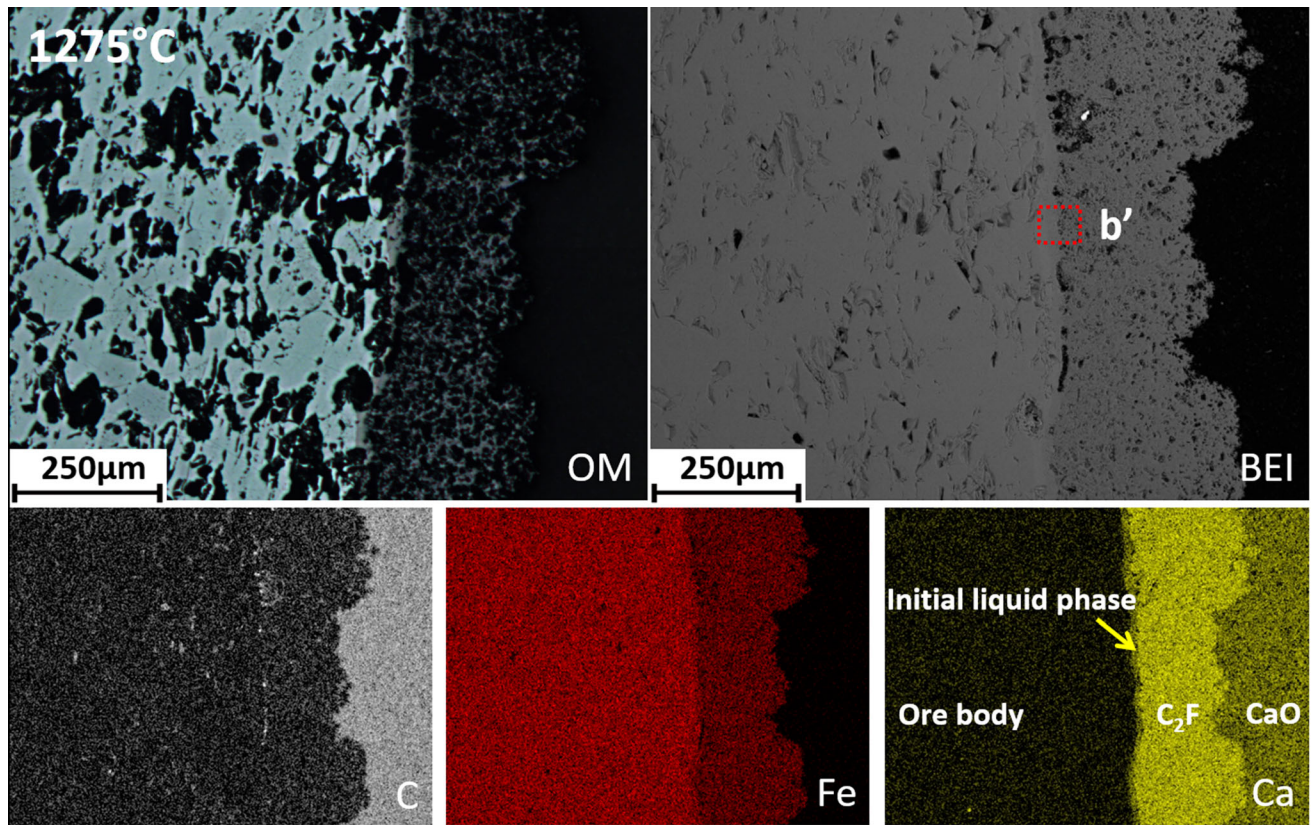


Fig. 5—Optical and BSE images and EDS mapping of C, Fe, and Ca distributions of area (b) in Figure 3.

of Fe and Ca along the line in Figure 6(a) are presented in Figure 6(b). To facilitate the assessment of chemical compositions of the mineral phases (*i.e.*, aid in phase identification), two parameters R and $C(\text{Fe}_2\text{O}_3)$ are introduced and included in Table III and Figure 6(b). These are defined by Eqs. 1 and 2.

$$R = \frac{n(\text{CaO})}{n(\text{Fe}_2\text{O}_3)} = \frac{n(\text{Ca})}{n(\text{Fe})/2} \quad [1]$$

$$C(\text{Fe}_2\text{O}_3) = \frac{n(\text{Fe}_2\text{O}_3)}{n(\text{Fe}_2\text{O}_3) + n(\text{CaO})} = \frac{1}{R + 1}, \quad [2]$$

where $n(i)$ is the molar fraction of species i . R takes a value of 0.5, 1, and 2 for CF_2 ($\text{CaO} \cdot (\text{Fe}_2\text{O}_3)_2$), CF ($\text{CaO} \cdot \text{Fe}_2\text{O}_3$), and C_2F ($(\text{CaO})_2 \cdot \text{Fe}_2\text{O}_3$), respectively. $C(\text{Fe}_2\text{O}_3)$ is the molar fraction of Fe_2O_3 which helps identify the position of components in a Fe_2O_3 - CaO phase diagram.

From Figure 6(b), for the thin middle layer of $\sim 20 \mu\text{m}$, even though R changes gradually, in general it is close to 0.5, corresponding to the composition for CF_2 . EDS analysis of Sites 4 and 5 within this layer gives similar compositions. The part of the EDS line scan within the right-hand side layer shows two sections with R equal to 1.5 and 2, respectively, with the latter corresponding to CF_2 . Sites 1, 2, and 3 located in the right-hand side layer were analyzed by EDS. Site 1, which is located in the slightly brighter phase, had a

composition corresponding to CF . Site 2 had a CaO content greater than C_2F . Site 3 had a composition between CF and C_2F . In the iron ore region, at the left-hand side in Figure 6(b), the Ca content gradually decreased with distance into the particle as a result of solid-state diffusion of CaO into the ore. The transfer of CaO into the interior of the ore particle means that Ca^{2+} ions have higher mobility than Fe^{3+} , as supported by previous research findings.^[9]

Figure 7 shows the phase diagram of the CaO - Fe_2O_3 system under 0.5 kPa O_2 in the gas phase, calculated using Factsage 7.0. The lowest temperature of liquid phase formation in the system is at the eutectic temperature, between CF and CF_2 , *i.e.*, 1208 °C (point M). It should be noted that since there was almost no liquid phase formed during the experiment at 1250 °C (Figure 3), the heating time may have been too short for reaction between CaO and Ore A. However, at 1275 °C, the thin middle layer of $\sim 20 \mu\text{m}$ (Figure 6(b)) and the major components in the right-hand side layer were in a liquid state.

This indicates that an initial liquid phase (ILP), as represented by the thin middle layer, was generated at the interface between the iron ore and CaO . The liquid phase penetrated into the CaO layer *via* the voids among fine CaO particles, and CaO started to dissolve into the liquid phase. When the dissolution of CaO reached saturation, solid C_2F was formed. Simultaneously, under a concentration gradient, CaO diffused to the iron ore interface through the liquid, reacting with the

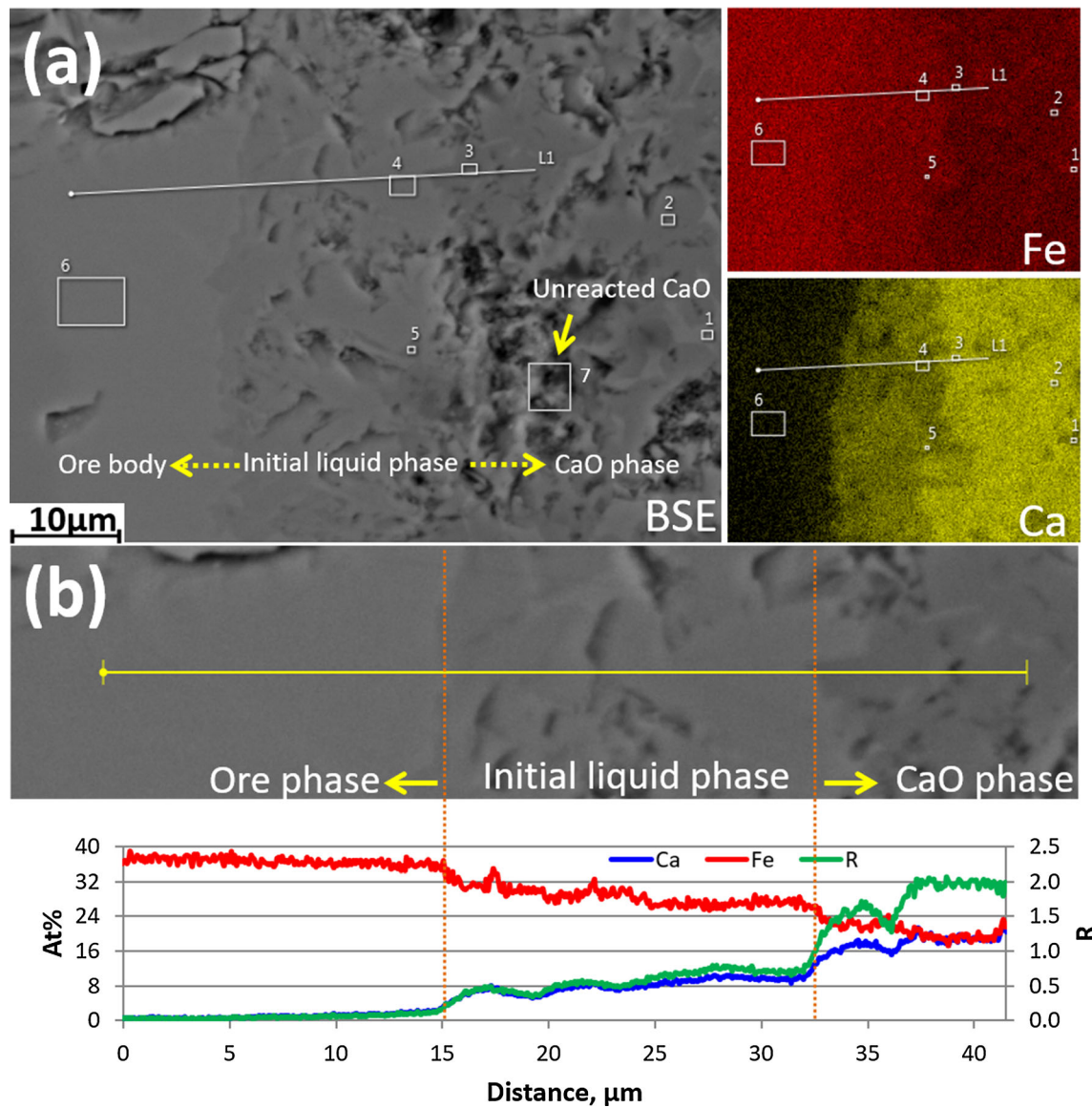


Fig. 6—(a) BSE image and EDS mapping of area b' in Figure 5; (b) the distributions of Ca, Fe, and R along the line marked in (a).

Table III. Elemental Composition (At. Pct) and Corresponding Phases at the Sites Marked in Figure 6(a)

Site	1	2	3	4	5	6	7
O	62.9	63.1	61.1	62.9	61.5	61.7	63.0
Al	0.02	0.05	0.10	0.10	0.14	0.07	0.17
Si	0.06	0.05	0.00	0.03	0.07	0.00	0.40
Ca	11.9	19.7	17.4	10.0	14.2	0.39	20.6
Fe	25.1	17.0	21.4	27.0	24.1	37.8	15.8
Total	100	100	100	100	100	100	100
R	0.95	2.32	1.62	0.74	1.17	0.02	2.61
C(Fe ₂ O ₃)	0.51	0.30	0.38	0.57	0.46	0.98	0.28

ore to form more liquid. The product layer of ~ 250 μm thickness is likely to have formed as a result of the CaO layer being penetrated by the initial liquid phase. After

cooling, it contained unreacted CaO, C₂F, and a solidified liquid phase. As already noted, the unreacted CaO exposed at the surface was lost during sample preparation, forming the pores observed in Figure 6(a). Some local sites in the liquid phase, such as Site 2 in Figure 6(a), had R values greater than 2, most likely due to suspended CaO particles.

Figure 8(a) shows the BSE image and EDS mapping of C, Fe, and Ca distributions in area (c) in Figure 3. As shown in Figure 8(a), three different regions were observed at the interface of the sample heated to 1300 °C, similar to phase evolution for the sample heated to 1275 °C (Figures 5 and 6). More pores were observed in the right-hand side layer due to the loss of unreacted CaO powder. The large pores were also observed at the interface because the liquid phase penetrated into fine pores and the fine pores between reacted CaO particles and in ore body accumulated under the effect of liquid surface tension.

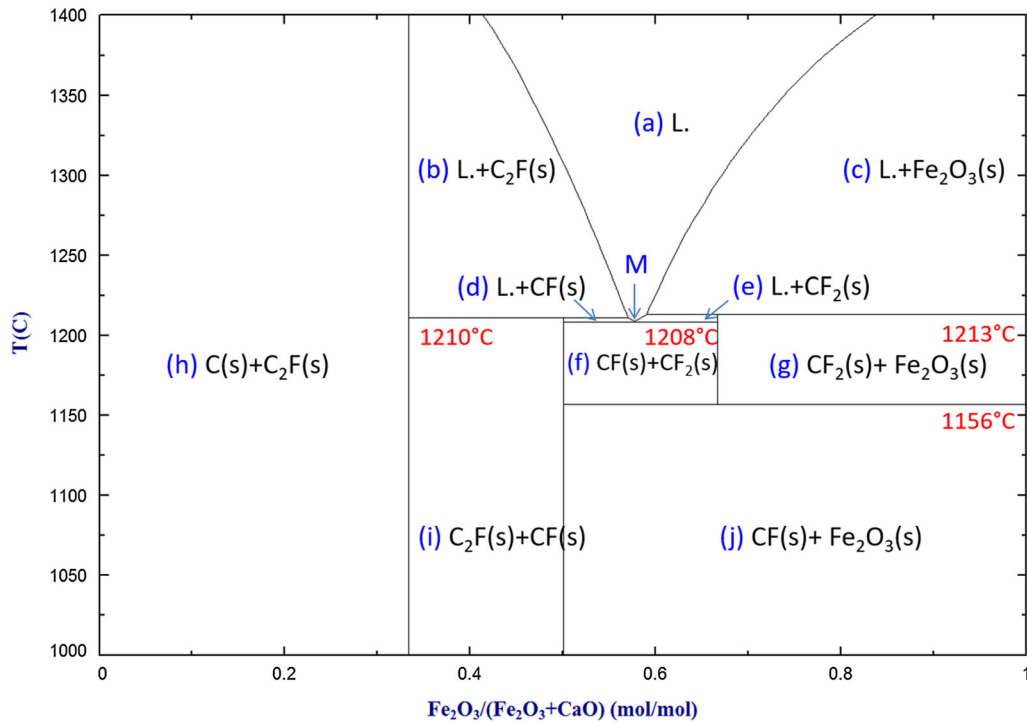


Fig. 7— Fe_2O_3 -CaO phase diagram at 0.5 kPa O_2 as calculated by Factsage 7.0.

The results of EDS analysis on the local sites marked in Figure 8 are shown in Table IV. Site 4 located in the middle layer had a composition close to that of the liquidus line in equilibrium with C_2F at 1300 °C (Figure 7). The liquid composition was likely to be time-dependent during sintering, determined by the supply of CaO through diffusion and its dilution by dissolving more iron oxides from the ore particle. Within the residual ore particle, although it contained little CaO (Sites 1 and 2), some discontinuous bands containing Ca can be observed in the Ca distribution mapping. These bands were formed by the penetration of liquid phase into the ore particle through pores and the formation of CF_2 via the reaction of the liquid with ore (composition in zone (g) in Fe_2O_3 -CaO phase diagram, Figure 7). The discontinuity of the bands is likely to be as a result of the inherent pore structure. Site 5 in the right-hand side layer, *i.e.*, the original CaO layer with penetrating liquid phase, shows a composition rich in Ca likely resulting from unreacted CaO. Site 6 in original CaO area shows the liquid phase penetrating into CaO.

Figure 8(b) shows the BSE image of area (c') in Figure 8(a) at higher magnification. It includes unreacted CaO, C_2F crystals (Sites C3 and C4, precipitated from liquid phase) and glass phase (Sites C1 and C2) from quenched liquid. Figure 8(c) shows the magnified BSE image of area (d) in Figure 3 from the sample heated to 1300 °C which was well away from the ore-CaO interface. Both the morphological structure and mineral composition were similar to those of area

(c') in Figure 8(b). It included crystallized C_2F (darker areas shown as Sites D2, D4, and D5) precipitated from liquid phase (glass phase after quenching, Site D3) and enclosed CaO clusters (Site D1).

Based on the previous analysis and discussion, the interaction mechanism between the hematite phase in Ore A and CaO flux is summarized in Figure 9. The interaction process progresses in three stages with temperature increase.

1. The interaction between hematite and CaO is relatively minor at low temperatures (< 1225 °C). There was insignificant diffusion of CaO into the ore particle, with no liquid phase formation observed at 1250 °C.
2. With increasing temperature, an initial liquid phase ($R = \sim 0.74$, $C(\text{Fe}_2\text{O}_3) = \sim 0.58$) is generated and penetrates into the CaO layer and ore particle *via* pores. Due to the fine powder nature of CaO, penetration velocity of the initial liquid layer into CaO is much faster than that into the ore particle.
3. CaO diffuses *via* the liquid phase from the CaO layer into the layer of initial liquid phase. The hematite ore dissolves into the initial liquid phase. This provides more liquid phase to penetrate into the CaO layer and ore particle. Simultaneously, C_2F forms from the reaction of CaO and the penetrated liquid, and CF_2 forms from the reaction between this liquid and internal ore body. Time permitting the process proceeds until either CaO or the ore is consumed.

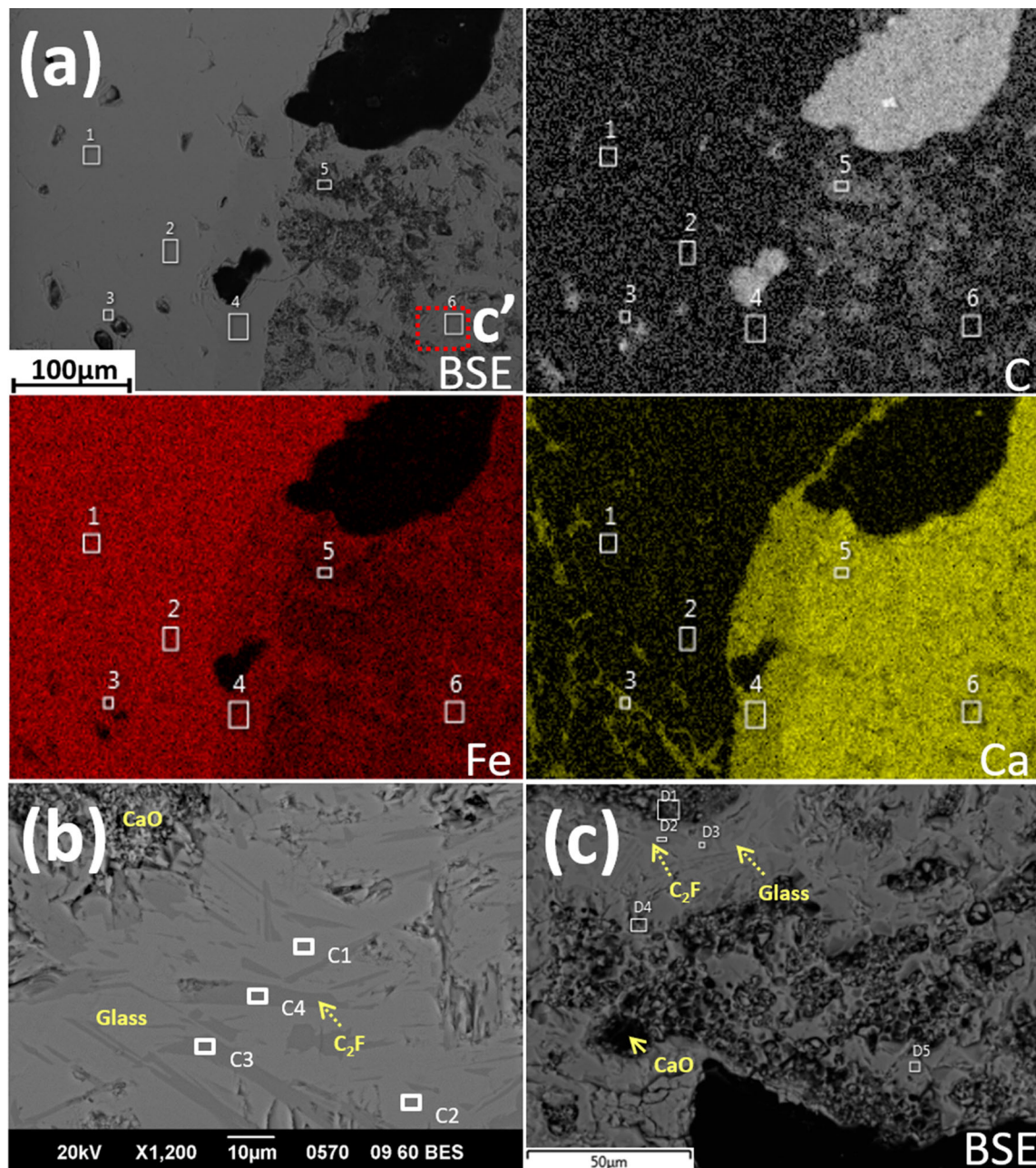


Fig. 8—(a) BSE image and EDS mapping of C, Fe, and Ca in area (c) in Figure 3; (b) higher magnification of BSE image of area (c') in (a); (c) BSE image of area (d) in Figure 3.

2. Hematite and MgO

The interaction between ore phase and MgO was investigated at 1250, 1275, and 1300 °C, and the results showed little interaction at temperatures under 1300 °C. Figure 10 shows the EDS line scan of the Fe and Mg contents across a crack of the ore cube surrounded by MgO in a sample heated up to 1300 °C. The EDS image does not show any sign of liquid phase generation. Instead, there were stripes of some reaction products from the surface of the ore particles. The Fe and Mg distributions along the line show that the distance of MgO diffusion *via* Mg²⁺ and O²⁻ into ore particles was approx. 60 μm. Within approx. 10 to 20 μm from the

interfaces, the Mg/Fe molar ratio was close to 1/3, which decreased with the increase of the distance from the interface. Some dark stripes were observed in both ore particles. These data illustrate that solid solution (Fe, Mg)O•Fe₂O₃ was formed due to the interaction between hematite and MgO *via* solid-state diffusion. In the solid-state reaction, the Mg²⁺ and Fe²⁺ ions could be exchanged since Fe₃O₄ and MgO•Fe₂O₃ have the same spinel structure.^[18] Overall, there was limited interaction between hematite in Ore A and MgO as no liquid phased was formed. Therefore, in this binary interaction without involvement of other fluxing materials, it is anticipated that MgO takes a negligible role in

Table IV. Elemental Composition (At. Pct) at the Sites Marked in Figure 8

Site	1	2	3	4	5	6	C1	C2	C3	C4	D1	D2	D3	D4	D5
O	61.7	61.3	59.6	60.5	62.2	61.1	60.7	60.1	58.8	59.6	63.0	61.9	63.9	60.9	61.0
Al	0.08	0.14	0.17	0.04	0.28	0.08	0.1	0.08	0.07	0.11	0.17	0.07	0.05	0.07	0.10
Si	0.11	0.01	0.05	0.04	0.29	0.00	0.05	0.03	0.06	0.10	0.40	0.11	0.01	0.11	0.09
Ca	0.00	0.03	6.58	12.6	23.3	13.6	10.4	10.4	20.0	20.1	20.6	19.1	8.30	19.9	19.8
Fe	38.1	38.5	33.6	26.9	14.0	25.3	28.7	29.3	21.1	20.1	15.8	18.8	27.7	19.1	19.0
Total	100	100	100	100	100	100	100	100	100	100	100	100	100	100	100
R	0.00	0.00	0.39	0.94	3.33	1.07	0.73	0.71	1.90	2.01	2.61	2.04	0.60	2.08	2.08
C(Fe ₂ O ₃)	1.00	1.00	0.72	0.52	0.23	0.48	0.58	0.58	0.34	0.33	0.28	0.33	0.63	0.32	0.32

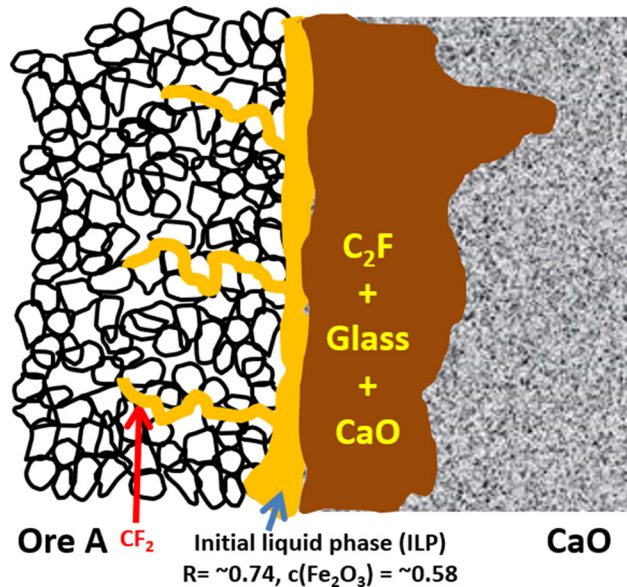


Fig. 9—Schematic of interaction between Ore A and CaO during sintering.

initial liquid phase formation during sintering in this experiment. The lack of liquid phase formation is consistent with the phase diagram between the two components.^[19] It is noted that MgO is considered a detrimental oxide in sintering that hinders CaO diffusion, increases temperature of the initial liquid phase and viscosity of liquid phase formed, and deteriorates the strength of the sinter product.^[20,21]

3. Hematite and SiO₂ or Al₂O₃

Figure 11 (a) and (b) shows the BSE images and EDS mapping of areas of Ore A in contact with SiO₂ and Al₂O₃, respectively, after heating to 1300 °C. No liquid phase formation was observed, with solid-state diffusion limited to ~ 5 μm from the interface. The formation of a solid product layer between Fe₂O₃ and SiO₂ and between Fe₂O₃ and Al₂O₃ was confirmed by the site EDS analysis (Table V). According to the binary phase diagrams,^[19] Fe₂O₃ and SiO₂ could form a liquid phase above 1177 °C only in a strong reducing atmosphere when Fe₂O₃ is reduced to FeO. A liquid phase between Fe₃O₄ and SiO₂ could not form below 1455 °C in air. Fe₂O₃ and Al₂O₃ could form solid solutions with

different compositions; according to the phase diagram, liquid phase formation seems impossible at 1300 °C.^[19] Therefore, according to the current experimental observations, SiO₂ and Al₂O₃ do not appear to play a significant role in initiation and formation of a liquid phase.

B. Interaction Between Mineral Phases in Ore B and Fluxing Materials

1. Mineral phases and CaO

Figure 12 presents the changes in morphology of Ore B in contact with CaO and heated to temperatures from 1225 °C to 1300 °C. The original ore has a stratiform structure of hematite/martite and goethite. After heating to 1225 °C, dehydration took place in the goethite layer, forming a porous structure, which caused a color change from light to dark gray under optical microscope, but no apparent liquid phase formed at the interface between CaO and the ore body. A typical morphology of the reaction interface (area (a)) is shown in Figure 13(a). The corresponding EDS mapping of the Ca distribution shows the diffusion of Ca into the ore particle was very limited, probably *via* solid state at this low temperature.

Figure 13(b) presents the BSE image and the EDS mapping of the distributions of different elements in the area (b) marked on the sample heated to 1250 °C. When temperature was increased to 1250 °C, a large amount of liquid phase was generated at the interface of the ore particle and penetrated into the porous layer of dehydrated goethite (Sites B1 and B2 in Table VI). Notably, the liquid phase started to penetrate into some sites (e.g., Sites B3 and B4) in the hematite layer where a low melting temperature phase was formed. From Figure 13(b), the preferable location of reaction was the porous layer of dehydrated goethite, where the initial liquid phase formed at the ore-CaO interface could be reached *via* the capillary effect.^[22,23] In addition, the finely distributed quartz, shown in Si mapping of the ore body in Figure 13(b), is highly reactive with CaO, which helps lower the melting point of goethite phase according to the phase diagrams.^[19] It is known that CaO and SiO₂ have high affinity; however, Sites B5 and B6, which represent quartz distributed in the hematite layer, did not show reaction with CaO. It is apparent that CaO did not reach these SiO₂-rich sites. The penetration of liquid phase *via* the porous structure was the major mechanism of mass transfer of CaO into the hematite layer. The

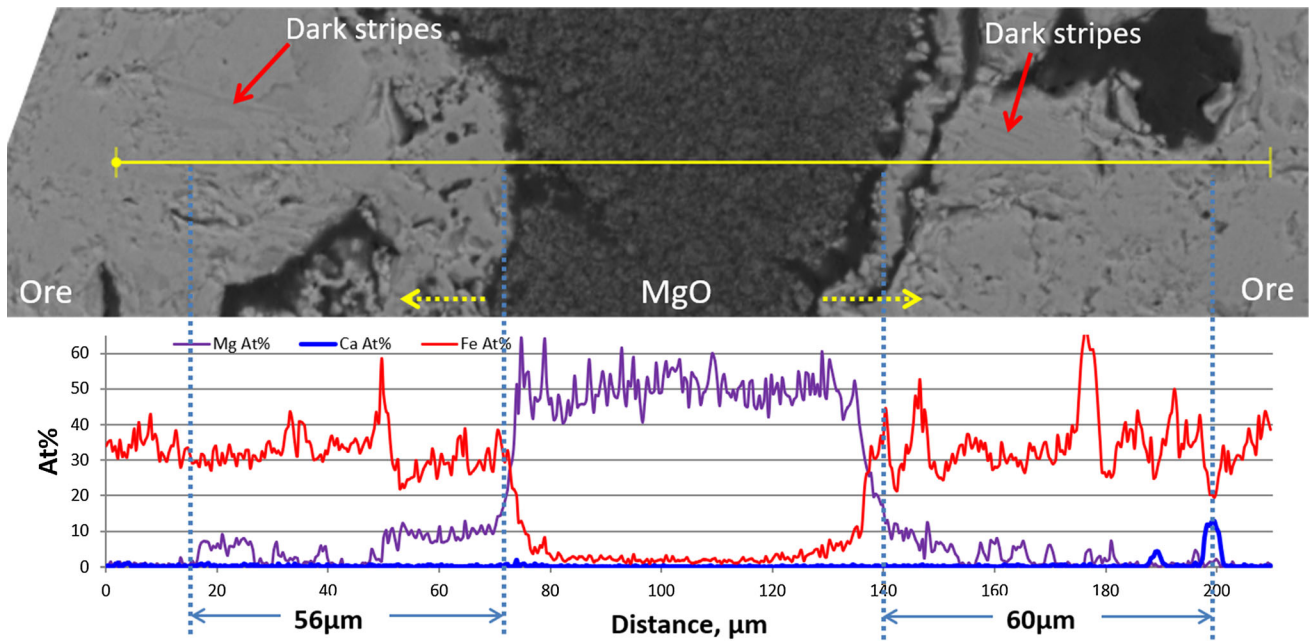


Fig. 10—Fe, Mg, and Ca distributions by a line scan across two Ore A particles with filled MgO heated to 1300 °C.

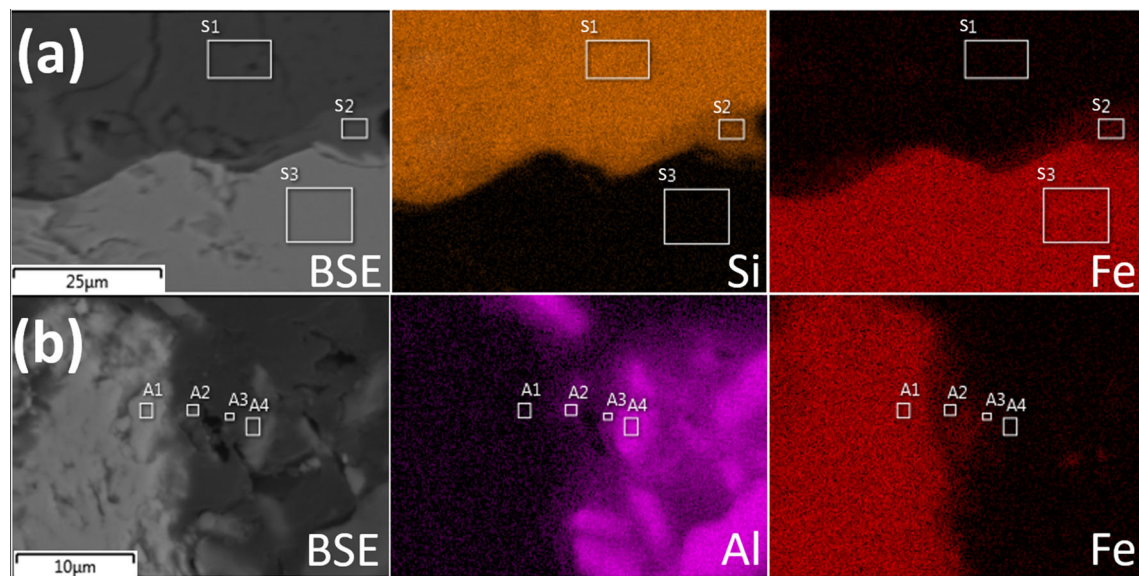


Fig. 11—BSE images and EDS mapping of element distributions of (a) Ore A-SiO₂ pair and (b) Ore A-Al₂O₃ pair heated to 1300 °C.

Table V. Elemental Composition (At. Pct) at the Sites Marked in Figure 11

Site	S1	S2	S3	A1	A2	A3	A4
O	67.3	67.1	61.2	61.3	25.3	57.0	63.8
Al	0.05	0.14	0.12	0.36	40.7	34.3	35.3
Si	32.5	25.3	0.08	0.57	1.02	1.15	0.23
Ca	0.02	0.04	0.03	0.09	0.40	0.23	0.03
Fe	0.20	7.49	38.6	37.7	32.6	7.29	0.62
Total	100	100	100	100	100	100	100

liquid phase provided a path for fast transport of CaO. However, not all the pores in the hematite layer were reached by CaO, perhaps because they were not connected with the zones of liquid phase formation.

As shown in Figure 12, when the temperature reached 1300 °C, the whole ore particle had melted, and the liquid phase penetrated into CaO. In Figure 12, a stripe-like structure was observed in area (c). Figure 13(c) presents the BSE image and the EDS mapping of the distributions of different elements. Similar to previous observations, the dark areas in the BSE image in Figure 13(c) resulted from the loss of enclosed CaO

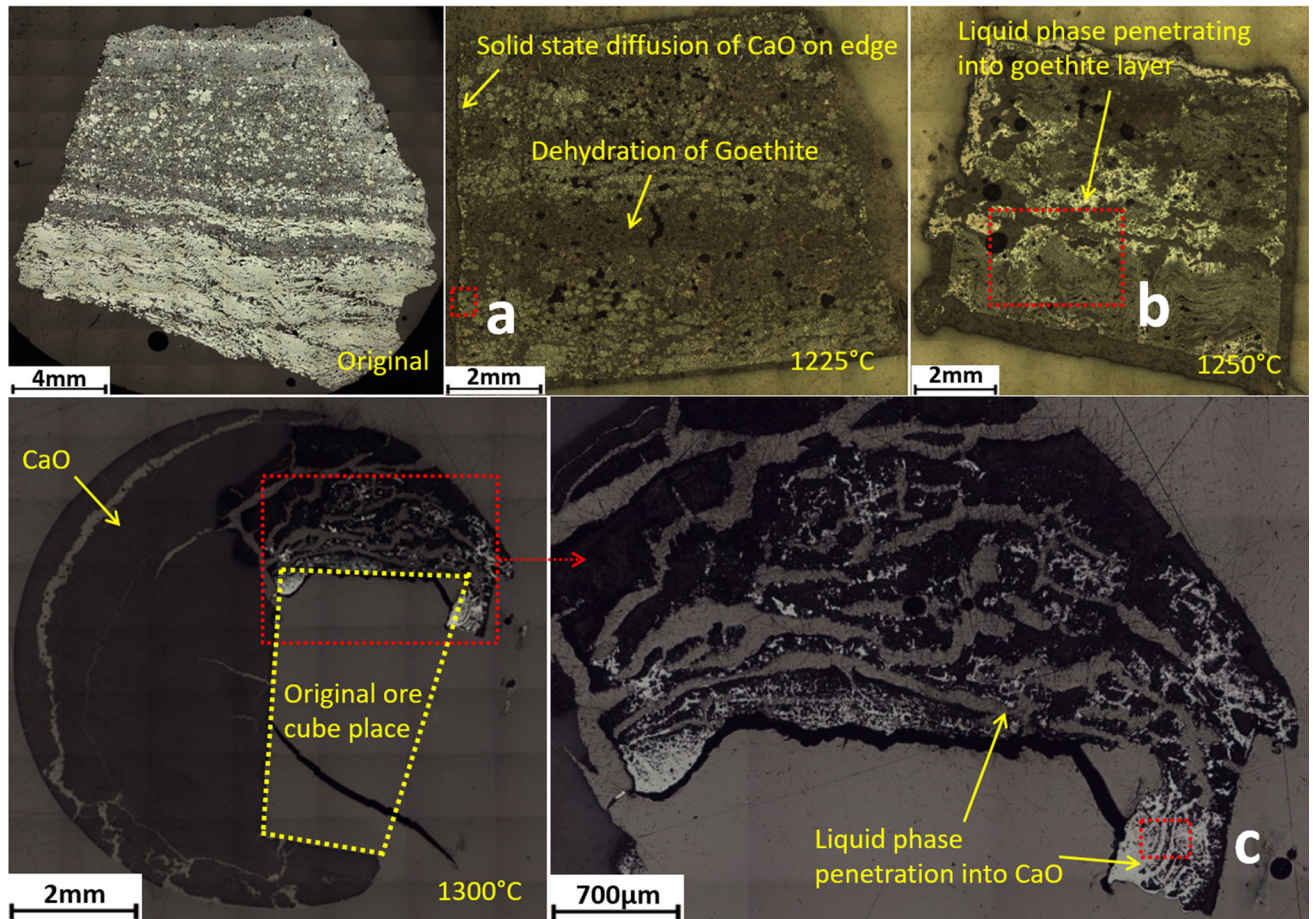


Fig. 12—Photomicrographs of Ore B-CaO tablet heated to different temperatures.

during sample preparation. The gray stripes with brighter precipitates in the BSE image were new phases resulting from the liquid phase penetrating into CaO. According to the EDS analysis (Table VI), the gray phase (Sites C1 and C2) had a chemical composition equivalent to C_2F , and the brighter precipitates (Sites C3 and C4) were silico-ferrite of calcium and aluminum (SFCA).^[24,25]

Compared with Ore A (predominately hematite), the presence of goethite and hematite in a layered structure is the most significant feature of Ore B. The transformation of goethite into hematite with a porous morphology provides favorable conditions for liquid phase penetration during the sintering process, so Ore B is likely to have better assimilation than Ore A. The proposed mechanism of interaction between Ore B and CaO during sintering is presented schematically in Figure 14, and is described as follows.

1. Dehydration of goethite takes place. CaO diffuses into the ore particle by solid-state diffusion, followed by initial liquid phase formation.
2. The initial liquid phase penetrates into the dehydrated, porous goethite layer. CaO diffuses through the liquid phase together with more liquid penetration into the goethite layer, which promotes disso-

lution of iron ore, forming more liquid phase; the liquid phase further penetrates into the hematite layers in the ore particle.

3. The initial liquid phase at the ore-CaO interface also penetrates into the CaO layer, enhancing the dissolution of CaO into liquid and diffusion of CaO towards the ore particle. C_2F and CF or glass phases form in the CaO layer.
4. If time allows, the process progresses until either ore or the flux is completely consumed.

C. Mineral phases and MgO

Figure 15 shows a photomicrograph of an Ore B cube with surrounding MgO, heated to a temperature of 1300 °C. A detailed analysis of local areas is also provided, by BSE observation and EDS mapping of Mg distribution. No changes were observed in the optical image except for dehydration of the goethite layer. In the area marked as (a), the BSE image and Mg distribution mapping in Figure 15(a) show that interaction seemingly took place within about 200 μm from the interface. However, the EDS analysis shows that the bright part represented by Sites A1 and A2 was MgO pressed into the ore particle with a small fraction of diffused Fe, and the layer in which Sites A3 and A4 were

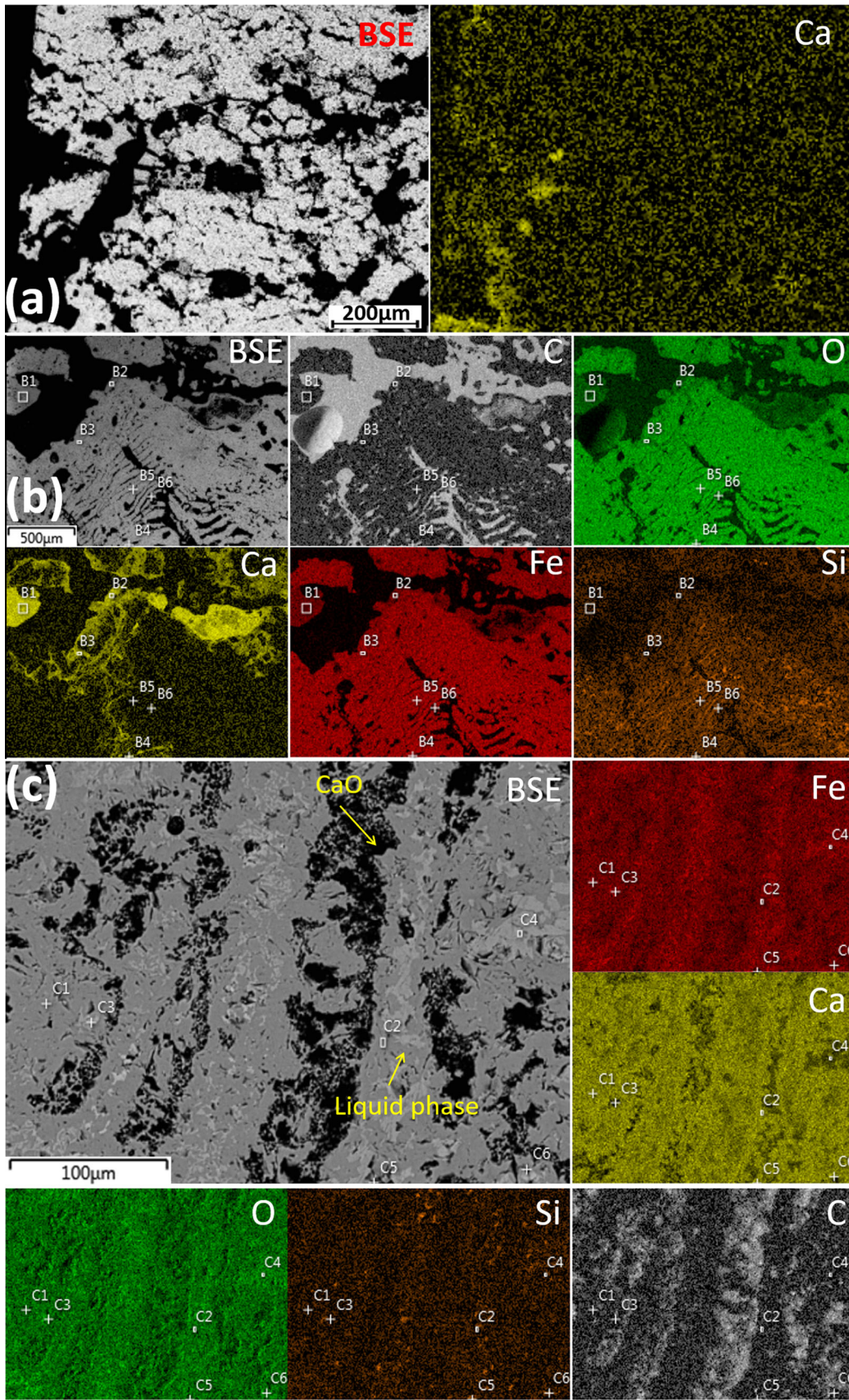


Fig. 13—BSE, EDS mapping of areas (a) to (c) in Figure 12.

Table VI. Elemental Composition (At. Pct) at the Sites Marked in Figures 13(b) and (c)

Site	B1	B2	B3	B4	B5	B6	C1	C2	C3	C4	C5	C6
O	55.3	54.9	54.7	62.8	59.6	56.1	52.6	52.4	52.7	50.7	65.1	52.2
Al	0.44	0.47	0.60	0.06	0.27	0.06	0.38	0.60	0.35	0.34	0.26	0.36
Si	0.50	0.62	1.18	7.12	34.4	31.5	0.45	0.41	0.24	0.04	6.56	8.56
Ca	19.2	17.9	14.0	12.6	0.47	0.14	23.5	23.5	6.30	11.8	21.1	27.7
Fe	24.6	26.1	29.5	17.4	5.31	12.2	23.1	23.1	40.4	37.1	6.90	11.2
Total	100	100	100	100	100	100	100	100	100	100	100	100
R	1.56	1.38	0.95	1.45	0.18	0.02	2.03	2.04	0.31	0.63	6.14	4.93
c(Fe ₂ O ₃)	0.39	0.42	0.51	0.41	0.85	0.98	0.33	0.33	0.76	0.61	0.14	0.17

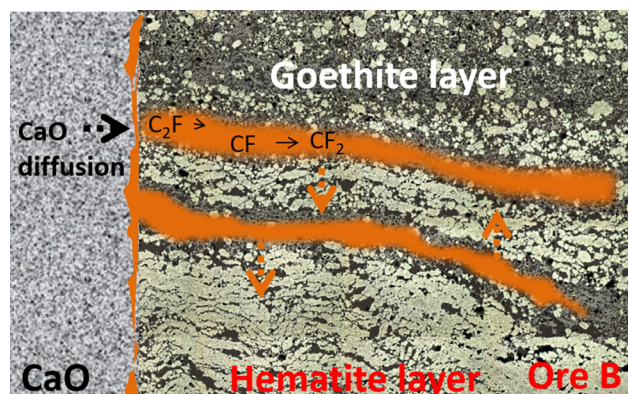


Fig. 14—Schematic diagram of the interaction between Ore B and CaO during sintering.

located was the product of MgO diffusion into ore particle with composition close to MgO·Fe₂O₃ (Table VII). The BSE image and Mg distribution in area (a') show that further diffusion of MgO in the hematite layer took place. A spinel-type solid solution was formed in local zones in the hematite layer (Sites A'3 and A'4), where the content of Al was higher than at other locations (Sites A'1 and A'2) because the high affinity between MgO and Al₂O₃ allows spinel to form.^[26]

The BSE image and Mg distribution of area (b) in Figure 15 show that MgO diffusion into hematite and goethite layers progressed differently. In the hematite layer (left-hand side in area b), 20 to 25 μm of ore was fully converted to MgO-Fe₂O₃ solution. In contrast, up to 50 μm of ore was fully converted in the goethite layer. The concentration of Mg in the hematite layer rapidly decreased with distance from the interface, and became negligible at Sites B1 and B2. The diffusion in the goethite layer was much greater, as most of the hematite ore in the layer was converted to MgO-Fe₂O₃ solution, but the penetration was decreased by the cavity generated due to ore dehydration. The faster diffusion in the goethite layer can be attributed to the porous yet contiguous morphology of the sintered goethite which increased the surface area where solid diffusion took place,^[27,28] and its relatively higher content of impurities which may have promoted formation of a liquid solution with MgO.^[26]

D. Mineral phases and Al₂O₃ or SiO₂

In the interaction experiments of Ore B with Al₂O₃ and SiO₂, no new mineral phase formation was observed at the interface of ore-flux pairs heated to 1300 °C. The observations show the inert behavior of Al₂O₃ and SiO₂ in respect to interactions with goethite and hematite without involvement of other fluxing materials.

The results of interaction between different mineral phases in iron ores and various fluxing materials reflected the processes of solid-state diffusion and initial liquid phase formation before a large amount of liquid phase can be generated. This investigation fills a knowledge gap concerning the interaction between the mineral phases of representative hematite ores and flux materials (CaO, MgO, Al₂O₃, and SiO₂). The study helps to better understand the mechanism of the sintering process and the behavior of ore mineral phases during iron ore matching in sinter plant, and can support the industry in the development of better condition to energy optimization and better usage of limestone, Mg-bearing raw materials and insights about quality.

IV. CONCLUSIONS

Based on the examination of the interaction between different mineral phases in iron ores and various fluxing materials, the following conclusions are drawn.

1. CaO was the most effective flux, generating an initial liquid phase by reacting with iron ore. With hematite and CaO, the formation of initial liquid phase begins above 1250 °C, while for hematite ore containing some goethite minerals, interaction between dehydrated goethite and CaO becomes effective at a lower temperature, between 1225 and 1250 °C, which promotes the sintering of hematite mineral phase.
2. The penetration of the initial liquid phase into the pores of ore particles plays an important role in the sintering process. The liquid provides a path for the mass transfer of flux into the iron ore particles, promoting further reaction and further liquid formation.
3. The formation of the initial liquid phase between dehydrated goethite and CaO was attributed to finely distributed quartz, while the porous morphology of dehydrated goethite facilitates the penetration of

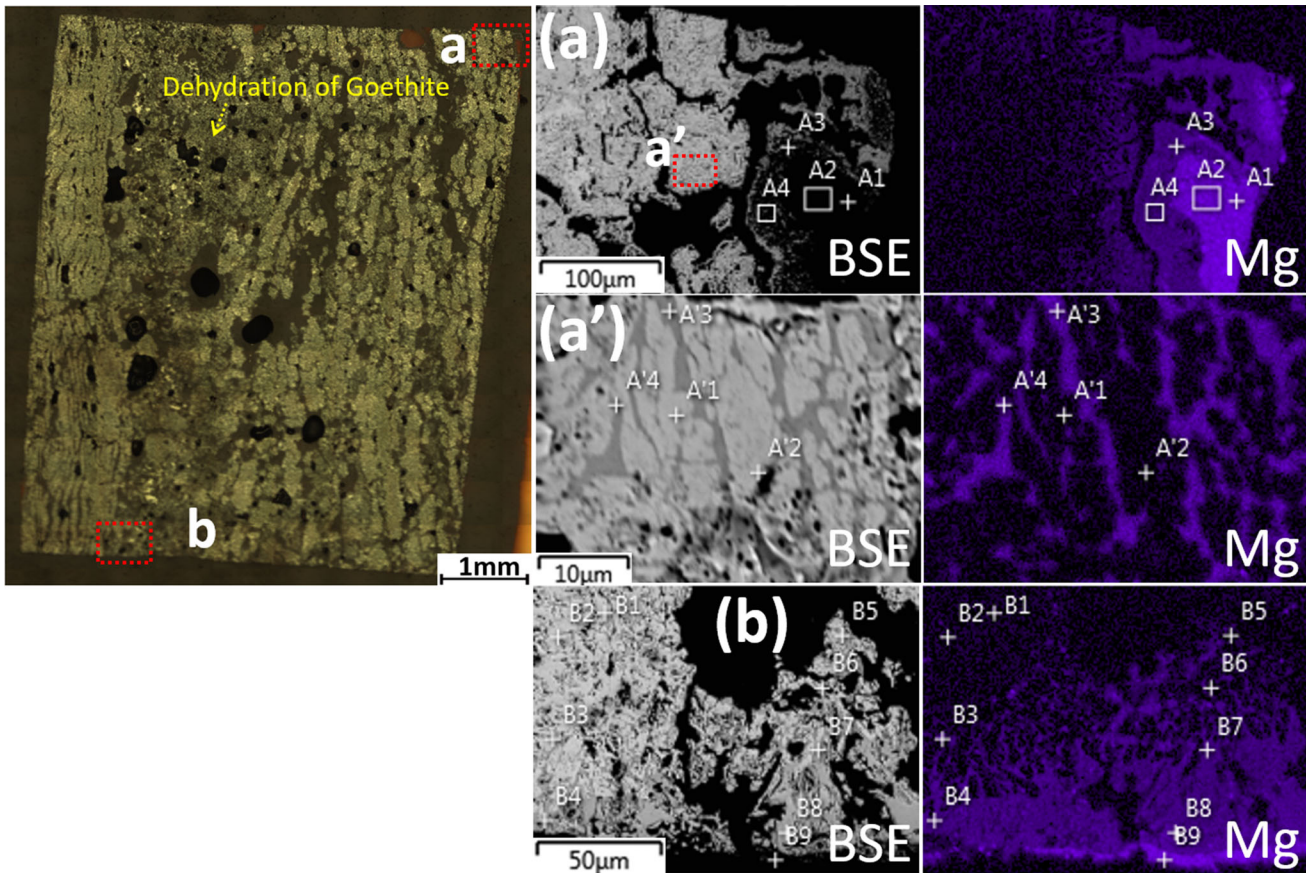


Fig. 15—Photomicrographs of Ore B heated with MgO until 1300 °C, and detailed analysis of local areas (a) (a') and (b) by BSE and EDS mapping of Mg distribution. (a) Upper right of the ore cube; (a') Rectangle area in (a); (b) Lower left of the ore cube.

Table VII. Elemental Composition (At. Pct) at the Sites Marked in Figure 15

Site	A1	A2	A3	A4	A'1	A'2	A'3	A'4
O	47.7	47.3	52.8	52.7	60.0	58.1	57.8	58.8
Mg	45.1	45.6	15.0	14.3	0.55	0.02	11.0	9.37
Al	0.00	0.00	0.04	0.00	0.50	0.26	1.20	1.10
Si	0.11	0.06	0.13	0.18	0.06	0.19	0.17	0.23
Ca	0.05	0.02	0.12	0.12	0.05	0.05	0.09	0.17
Fe	7.10	7.05	32.0	32.7	38.9	41.3	29.8	30.4
Total	100	100	100	100	100	100	100	100

Site	B1	B2	B3	B4	B5	B6	B7	B8	B9
O	60.0	60.2	57.5	55.5	58.8	59.8	57.2	57.8	58.1
Mg	0.09	0.05	11.8	10.5	0.10	0.03	10.8	11.0	24.9
Al	0.09	0.03	0.10	0.12	1.77	1.52	1.46	0.28	0.05
Si	0.25	0.21	0.30	0.17	0.25	0.10	0.07	0.13	13.8
Ca	0.00	0.04	0.22	0.24	0.19	0.12	0.09	0.27	2.56
Fe	39.6	39.5	30.1	33.5	38.9	38.5	30.4	30.6	0.56
Total	100	100	100	100	100	100	100	100	100

liquid into the goethite layer. The liquid can then further penetrate into the hematite layer, enhancing the interaction between the ore and flux. As a result,

Ore B in the investigation shows higher assimilation with CaO than Ore A.

- MgO diffuses into hematite ores by solid-state diffusion and forms a solid solution $(\text{Fe, Mg})\text{O}\cdot\text{Fe}_2\text{O}_3$. The interaction of hematite and dehydrated goethite with MgO is limited. The diffusion of MgO in a porous but continuous dehydrated goethite matrix is relatively faster than in the denser hematite phase. However, a cavity or crack caused by dehydration can retard or block solid phase diffusion of Mg into an ore particle. In addition, the inherent impurities Al and Si are helpful for MgO diffusion to form spinel solid solution, which is not expected to play an important role in sinter process.
- Externally added Al_2O_3 and SiO_2 are relatively inert during sintering, and are expected to play little role without involvement of CaO.

ACKNOWLEDGMENTS

The authors gratefully acknowledge funding from the Australian Research Council Research Hub for Australian Steel Manufacturing (Project Number IH130100017) and the support of BlueScope Steel Ltd. The SEM/EDS observations were carried out at the

REFERENCES

1. J. Wang: *Metall. Eng.*, 2016, vol. 3, pp. 79–86.
2. S. Wu, H.L. Han, H.X. Li, J. Xu, S.D. Yang, and X. Liu: *Int. J. Miner. Metall. Mater.*, 2010, vol. 17, pp. 11–16.
3. Z. Xiao, L. Chen, Y. Yang, X. Li, and M. Barati: *ISIJ Int.*, 2017, vol. 57, pp. 795–804.
4. J. Clout and J. Manuel: *Powder Technol.*, 2003, vol. 130, pp. 393–99.
5. R. Morris and M. Kneeshaw: *Aust. J. Earth Sci.*, 2011, vol. 58, pp. 417–451.
6. C.E. Loo: *ISIJ Int.*, 2005, vol. 45, pp. 436–48.
7. C.E. Loo, L.T. Matthews, and D.P. O’dea: *ISIJ Int.*, 2011, vol. 51, pp. 930–38.
8. D. Debrincat and L. Ce: *ISIJ Int.*, 2004, vol. 44, pp. 1308–17.
9. X. Guo and Y. Ono: *Mem. Fac. Eng. Kyushu Univ.*, 1992, vol. 52, pp. 7–21.
10. H. Li: *ISIJ Int.*, 1989, vol. 29, pp. 24–32.
11. N. Oyama, T. Higuchi, S. Machida, H. Sato, and K. Takeda: *ISIJ Int.*, 2009, vol. 49, pp. 650–658.
12. Z. Wang, D. Pinson, S. Chew, B.J. Monaghan, H. Rogers, and G. Zhang: *ISIJ Int.*, 2016, vol. 56, pp. 505–12.
13. H. Li: *ISIJ Int.*, 1993, vol. 33, pp. 462–73.
14. E. Kasai, Y. Sakano, T. Kawaguchi, and T. Nakamura: *ISIJ Int.*, 2000, vol. 40, pp. 857–62.
15. H. Li, D. Pinson, P. Zulli, L. Lu, R. Longbottom, S. Chew, B. Monaghan, and G. Zhang: *Metall. Mater. Trans. B*, 2018, vol. 49B, pp. 2285–97.
16. H. Li-Heng and J.A. Whiteman: *ISIJ Int.*, 1989, vol. 29, pp. 24–32.
17. H. Li, D. Pinson, P. Zulli, L. Lu, R. Longbottom, S. Chew, B. Monaghan, and G. Zhang: *J. Hazard. Mater.*, 2019, vol. 385 (121592), pp. 1–13.
18. Y. Guo and X. Guo: *ISIJ Int.*, 2017, vol. 57, pp. 228–35.
19. V.D. Eisenhüttenleute and M. Allibert: *Slag atlas*, Verlag Stahleisen, Düsseldorf, Germany, 1995, p. 70.
20. Z. Wang, D. Pinson, S. Chew, H. Rogers, B.J. Monaghan, and G. Zhang: *ISIJ Int.*, 2016, vol. 56, pp. 1315–24.
21. S. Wu, H. Han, W. Jiang, L. Zhu, G. Feng, and Z. Zhang: *J. Univ. Sci. Technol. Beijing*, 2009, vol. 31, pp. 428–32.
22. E.W. Washburn: *Phys. Rev.*, 1921, vol. 17, pp. 273–83.
23. R.M. German: *Liquid Phase Sintering*, Springer, Berlin, 2013, pp. 13–41.
24. N.V. Scarlett, M.I. Pownceby, I.C. Madsen, and A.N. Christensen: *Metall. Mater. Trans. B*, 2004, vol. 35B, pp. 929–36.
25. A. Cores, A. Babich, M. Muñoz, S. Ferreira, and J. Mochon: *ISIJ Int.*, 2010, vol. 50, pp. 1089–98.
26. L. Ping, A. Azad, and T.W. Dung: *Mater. Res. Bull.*, 2001, vol. 36, pp. 1417–30.
27. R.J. Borg and G.J. Dienes: *An Introduction to Solid State Diffusion*, Elsevier, Oxford, 2012, pp. 24–52.
28. M.E. Brown, D. Dollimore, and A.K. Galwey: *Reactions in the Solid State*, Elsevier, Amsterdam, 1980, pp. 41–109.

Publisher’s Note Springer Nature remains neutral with regard to jurisdictional claims in published maps and institutional affiliations.